

Multi-band asymmetric transmissions based on bi-layer windmill-shaped metamaterial

Ying-Hua Wang(王英华), Jie Li(李杰), Zheng-Gao Dong(董正高), Yan Li(李妍), and Xu Zhang(张旭)
Citation: Chin. Phys. B, 2021, 30 (**11**): 114216. DOI: 10.1088/1674-1056/ac16d2
Journal homepage: http://cpb.iphy.ac.cn; http://iopscience.iop.org/cpb

What follows is a list of articles you may be interested in

Multi-band asymmetric transmissions based on bi-layer windmill-shaped metamaterial

Ying-Hua Wang(王英华), Jie Li(李杰), Zheng-Gao Dong(董正高), Yan Li(李妍), and Xu Zhang(张旭)
Chin. Phys. B, 2021, 30 (**11**): 114216. DOI: 10.1088/1674-1056/ac16d2

Solar broadband metamaterial perfect absorber based on dielectric resonant structure of Ge cone array and InAs film

Kuang-Ling Guo(郭匡灵), Hou-Hong Chen(陈厚宏), Xiao-Ming Huang(黄晓明), Tian-Hui Hu(胡天惠), and Hai-Ying Liu(刘海英)†
Chin. Phys. B, 2021, 30 (**11**): 114201. DOI: 10.1088/1674-1056/abf91e

Solar energy full-spectrum perfect absorption and efficient photo-thermal generation

Zhefu Liao(廖喆夫), Zhengqi Liu(刘正奇), Qizhao Wu(吴起兆), Xiaoshan Liu(刘晓山), Xuefeng Zhan(詹学峰), Gaorong Zeng(曾高荣), and Guiqiang Liu(刘桂强)
Chin. Phys. B, 2021, 30 (**8**): 084206. DOI: 10.1088/1674-1056/ac0696

Efficient realization of daytime radiative cooling with hollow zigzag SiO_2 metamaterials

Huawei Yao(姚华伟), Xiaoxia Wang(王晓霞), Huaiyuan Yin(殷怀远), Yuanlin Jia(贾渊琳), Yong Gao(高勇), Junqiao Wang(王俊俏), and Chunzhen Fan(范春珍)
Chin. Phys. B, 2021, 30 (**6**): 064214. DOI: 10.1088/1674-1056/abd697

Broadband asymmetric transmission for linearly and circularly polarization based on sand-clock structured metamaterial

Tao Fu(傅涛), Xing-Xing Liu(刘兴兴), Guo-Hua Wen(文国华), Tang-You Sun(孙堂友), Gong-Li Xiao(肖功利), and Hai-Ou Li(李海鸥)
Chin. Phys. B, 2021, 30 (**1**): 014201. DOI: 10.1088/1674-1056/abb662

Multi-band asymmetric transmissions based on bi-layer windmill-shaped metamaterial*

Ying-Hua Wang(王英华)[1,†], Jie Li(李杰)[2], Zheng-Gao Dong(董正高)[3], Yan Li(李妍)[1], and Xu Zhang(张旭)[1]

[1] School of Physics and Physical Engineering, Shandong Provincial Key Laboratory of Laser Polarization and Information Technology, Qufu Normal University, Qufu 273165, China

[2] Grünberg Research Centre, Nanjing University of Posts and Telecommunications, Nanjing 210023, China

[3] School of Physics, Southeast University, Nanjing 211189, China

(Received 19 April 2021; revised manuscript received 18 July 2021; accepted manuscript online 22 July 2021)

This study proposes a bi-layer windmill-shaped metamaterial that consists of resonators, with similar shapes, on both sides of a dielectric substrate. In this study, the second layer is rotated clockwise around the substrate normal at 90° and thereafter flipped in the first layer. Due to the introduction of a windmill-like shape, the resonant structures result in new resonant modes and thus can achieve multi-band high-efficiency cross-polarization conversions and asymmetric transmissions (ATs) for a linearly polarized incident plane wave with a maximum asymmetric parameter of 0.72. Depending on the geometric parameters of our windmill-shaped structures, the AT effects can be flexibly modulated in a broad multi-band from 160 THz to 400 THz, which has not been reported in previous studies. These outstanding AT effects provide potential applications in optical diodes, polarization control switches, and other nano-devices.

Keywords: metamaterial, multi-band, asymmetric transmission, polarization conversion

PACS: 42.25.Bs, 42.25.Ja, 42.79.Ci, 81.05.Xj **DOI:** 10.1088/1674-1056/ac16d2

1. Introduction

Metamaterials and metasurfaces have become an important research field because they present powerful capacities for manipulating the fundamental properties of the propagating electromagnetic waves due to the flexible design of subwavelength geometric shapes and sizes.[1,2] In addition, acoustic metamaterials are also proposed to investigate the transmission spectra and sound insulation performance.[3,4] Since the proposal of the concept of metamaterials, several novel structures have been reported, ranging from microwave to optical regimes, such as I-shaped metamaterials, split-ring resonators, L-shaped metallic antennas, and S-shaped holes.[5–9] Since then, many studies have paid attention to focusing beams,[10] creating orbital angular momentum,[11] and manipulating the polarization states, phases, and modes of TE/TM waves.[12,13] In 2007, Zhou *et al.* proposed an I-shaped metamaterial to manipulate the polarization of electromagnetic waves and achieved complete conversion between two perpendicular linear polarizations.[9] In 2020, broadband linear-to-circular polarization conversion was realized among reflected waves.[14] In addition, metamaterials have been used to realize perfect absorption, circular dichroism, optical activity, and the asymmetric transmission (AT) effect.[15–20]

In recent decades, the AT effect has garnered increasing attention. To realize outstanding and tunable AT effects in linearly and circularly polarized plane waves, several studies have been conducted, such as changing the shapes of symmetry-broken chiral metastructures,[21,22] increasing the layers of the proposed nanobars,[23,24] and tilting the rectangular nanoholes.[25] With regard to circularly polarized plane waves, high-efficiency broadband and dual-band AT effects have been studied and realized from microwave to optical regimes,[20,26–28] and tunable AT effects have also been realized by integrating the graphene layers with metamaterials.[29–31] With regard to linearly polarized plane waves, several studies have focused on enhancing the efficiency and broadening the band of the AT effect. In these studies, the AT effect in the microwave regime achieved better results than those in the optical regime. For instance, dual-band, broadband, and multi-band AT effects have been realized in the microwave regime with high efficiency.[21,32,33] In comparison with the microwave regime, most studies on the near-infrared regime have realized the broadband or dual-band AT effect with low efficiencies.[33–35] For example, Zhang realized both circularly and linearly polarized AT effects using one-layer metamaterials, but the AT values were about 0.1.[25,29] To increase the AT values, more works paid attention to bi-layer metamaterials, then I-L-shaped, S-shaped, split ring-shaped Ω-shaped metamaterial, and many other metamaterials were proposed, and the AT values increased to 0.8.[35–40] For further increases in AT effects, multilayer meta-

*Project supported by the National Youth Foundation of China (Grant Nos. 11904200 and 11704219), the National Natural Science Foundation of China (Grant No. 11774053), the Natural Science Foundation of Jiangsu Province, China (Grant No. BK20190726), the Natural Science Foundation of the Jiangsu Higher Education Institutions of China (Grant No. 18KJD140004), NJUPT-SF (Grant No. NY218099), and the Opening Project of the Shanghai Key Laboratory of Special Artificial Microstructure Materials and Technology (Grant No. hxkj2019007).

†Corresponding author. E-mail: wyh121@qfnu.edu.cn

© 2021 Chinese Physical Society and IOP Publishing Ltd

material has also been proposed and the AT values have been increased to 0.9. But here, the multilayer metamaterials increase the complexity and difficulty of the fabrication process, so it is necessary to enhance and broaden the AT effects using bi-layer metamaterials.[24,41,42] In previous works, the dual-band AT effect has also been realized by bi-layer metamaterial with a maximum of about 0.75,[8,32,43,44] but a few studies have reported the multi-band AT effect and its tunable properties. According to the multi-band absorption, multi-band polarization conversion, and multi-band circular dichroism and other multi-band electromagnetic effects, we know that it is useful to study the multi-band AT effect on the near-infrared regime.[45–47]

In this study, we propose a bi-layer windmill-shaped metamaterial and numerically investigate the multi-band AT effect and its tunable properties using the finite-difference time-domain method. In comparison with the split-ring resonator, the windmill-shaped resonators can motivate and enhance more resonant modes. Consequently, the simulated results demonstrate that the AT values are greater than 0.5 at 195, 260, and 309 THz. Moreover, the high-efficiency AT effects can be flexibly tuned by modulating the geometric parameters of the proposed metamaterial. For instance, the bandwidth can be tuned by changing the size s, whereas the polarization state of the transmitted plane wave can be tuned by changing the gap between the first and second layers. The additional operating frequency bands and tunable properties provide more application possibilities for the AT effect in the future.

2. Design and structure

Firstly, we discuss the principles of the bi-layer windmill-shaped metamaterial design. When a linearly polarized plane wave is propagating in the $+z$ direction, the illuminated and transmitted electric field can be given by[48,49]

$$\boldsymbol{E}_i(\boldsymbol{r},t) = \begin{pmatrix} i_x \\ i_y \end{pmatrix} \mathrm{e}^{\mathrm{i}(kz-\omega t)}, \tag{1}$$

$$\boldsymbol{E}_t(\boldsymbol{r},t) = \begin{pmatrix} t_x \\ t_y \end{pmatrix} \mathrm{e}^{\mathrm{i}(kz-\omega t)}, \tag{2}$$

and then the illuminated and transmitted electric fields can be connected by the Jones matrix $\boldsymbol{T}$

$$\begin{pmatrix} t_x \\ t_y \end{pmatrix} = \begin{pmatrix} T_{xx}^{\mathrm{f}} & T_{xy}^{\mathrm{f}} \\ T_{yx}^{\mathrm{f}} & T_{yy}^{\mathrm{f}} \end{pmatrix} \begin{pmatrix} i_x \\ i_y \end{pmatrix} = \boldsymbol{T}_{\mathrm{lin}}^{\mathrm{f}} \begin{pmatrix} i_x \\ i_y \end{pmatrix}. \tag{3}$$

Here, T_{xx}^{f} and T_{yx}^{f} indicate the x and y polarized transmission coefficients, when the x polarized incident plane wave propagates along the forward ($+z$) directions. Here, T_{xy}^{f} and T_{yy}^{f} indicate the x and y polarized transmission coefficients, when the y polarized incident plane wave propagates along the forward ($+z$) directions. If the metamaterial meets the reciprocity theorem, the backward ($-z$) direction transmission matrix $\boldsymbol{T}_{\mathrm{lin}}^{\mathrm{b}}$ can be described as follows:

$$\boldsymbol{T}_{\mathrm{lin}}^{\mathrm{b}} = \begin{pmatrix} T_{xx}^{\mathrm{b}} & T_{xy}^{\mathrm{b}} \\ T_{yx}^{\mathrm{b}} & T_{yy}^{\mathrm{b}} \end{pmatrix} = \begin{pmatrix} T_{xx}^{\mathrm{f}} & -T_{yx}^{\mathrm{f}} \\ -T_{xy}^{\mathrm{f}} & T_{yy}^{\mathrm{f}} \end{pmatrix}. \tag{4}$$

For circularly polarized plane waves propagating along the forward ($+z$) direction, the transmission matrix $\boldsymbol{T}_{\mathrm{circ}}^{\mathrm{f}}$ can be described by

$$\boldsymbol{T}_{\mathrm{circ}}^{\mathrm{f}} = \begin{pmatrix} T_{++}^{\mathrm{f}} & T_{+-}^{\mathrm{f}} \\ T_{-+}^{\mathrm{f}} & T_{--}^{\mathrm{f}} \end{pmatrix} = \frac{1}{2} \begin{pmatrix} T_{xx}^{\mathrm{f}} + T_{yy}^{\mathrm{f}} + \mathrm{i}(T_{xy}^{\mathrm{f}} - T_{yx}^{\mathrm{f}}) & T_{xx}^{\mathrm{f}} - T_{yy}^{\mathrm{f}} - \mathrm{i}(T_{xy}^{\mathrm{f}} + T_{yx}^{\mathrm{f}}) \\ T_{xx}^{\mathrm{f}} - T_{yy}^{\mathrm{f}} + \mathrm{i}(T_{xy}^{\mathrm{f}} + T_{yx}^{\mathrm{f}}) & T_{xx}^{\mathrm{f}} + T_{yy}^{\mathrm{f}} - \mathrm{i}(T_{xy}^{\mathrm{f}} - T_{yx}^{\mathrm{f}}) \end{pmatrix}. \tag{5}$$

Here, the T_{++}^{f} and T_{-+}^{f} indicate the right and left circularly polarized transmission coefficients, when the right circularly polarized incident plane wave propagates along the forward ($+z$) directions. The T_{+-}^{f} and T_{--}^{f} indicate the left and right circular polarized transmission coefficients, when the left circularly polarized incident plane wave propagates along the forward ($+z$) directions.

Then, the AT parameters for linearly and circularly polarized plane waves can be defined as

$$\begin{aligned} \Delta_{\mathrm{lin}} &= \left(\left|T_{xx}^{\mathrm{f}}\right|^2 + \left|T_{yx}^{\mathrm{f}}\right|^2\right) - \left(\left|T_{xx}^{\mathrm{b}}\right|^2 + \left|T_{yx}^{\mathrm{b}}\right|^2\right) \\ &= \left|T_{yx}^{\mathrm{f}}\right|^2 - \left|T_{xy}^{\mathrm{f}}\right|^2, \end{aligned} \tag{6}$$

$$\begin{aligned} \Delta_{\mathrm{circ}} &= \left(\left|T_{++}^{\mathrm{f}}\right|^2 + \left|T_{-+}^{\mathrm{f}}\right|^2\right) - \left(\left|T_{++}^{\mathrm{b}}\right|^2 + \left|T_{-+}^{\mathrm{b}}\right|^2\right) \\ &= \left|T_{-+}^{\mathrm{f}}\right|^2 - \left|T_{+-}^{\mathrm{f}}\right|^2. \end{aligned} \tag{7}$$

Here, the $\left|T_{xx}^{\mathrm{f}}\right|^2 + \left|T_{yx}^{\mathrm{f}}\right|^2$ and $\left|T_{xx}^{\mathrm{b}}\right|^2 + \left|T_{yx}^{\mathrm{b}}\right|^2$ mean the total transmittance for the x polarized incident plane wave propagating along the forward ($+z$) and backward ($-z$) directions, respectively. Similarly, $\left|T_{++}^{\mathrm{f}}\right|^2 + \left|T_{-+}^{\mathrm{f}}\right|^2$ and $\left|T_{++}^{\mathrm{b}}\right|^2 + \left|T_{-+}^{\mathrm{b}}\right|^2$ mean the total transmittance for a right polarized incident plane wave propagating along the forward ($+z$) and backward ($-z$) directions, respectively.

According to Eqs. (5)–(7) the AT effect can be realized in only linearly polarized plane waves, when $T_{xx} = T_{yy}$, and $\left|T_{xy}\right| \neq \left|T_{yx}\right|$.

To realize the $T_{xx} = T_{yy}$, and $\left|T_{xy}\right| \neq \left|T_{yx}\right|$, we propose a bi-layer windmill-shaped resonator, which is presented in Fig. 1. The second layer is rotated clockwise about the z-axis at 90° and then flipped along the x-axis with respect to the windmill-shaped structure in the first layer.[49] In addition, we rotate the (x, y, z) coordinate system about the z-axis by 45° to establish a coordinate system (x', y', z'). As a result, the bi-layer windmill-shaped resonator breaks all rotation symmetries, except the 180° rotation symmetry for the y'-axis. For the (x', y', z') coordinate system, the bi-layer windmill-shaped resonator

looks the same when x'/y' polarized plane waves propagate along the forward ($+z$-direction) or backward ($-z$-direction). Then we can get

$$T_{x'y'} = -T_{y'x'}. \tag{8}$$

Here, the (x, y, z) coordinate system and the (x', y', z') coordinate system can be connected by the Jacobi matrix $\boldsymbol{C}$, which is described as follows:

$$\begin{pmatrix} T_{x'x'} & T_{x'y'} \\ T_{y'x'} & T_{y'y'} \end{pmatrix} = \boldsymbol{C} \begin{pmatrix} T_{xx} & T_{xy} \\ T_{yx} & T_{yy} \end{pmatrix} \boldsymbol{C}^{-1}. \tag{9}$$

Here,

$$\boldsymbol{C} = \frac{\sqrt{2}}{2} \begin{pmatrix} 1 & -1 \\ 1 & 1 \end{pmatrix}. \tag{10}$$

According to Eqs. (8)–(10) we can get $T_{xx} = T_{yy}$. In addition, the windmill arms play an important role in inducing and enhancing multi-band resonances.[50] As a result, the bi-layer windmill-shaped resonator can result in a multi-band AT effect for only linearly polarized plane waves.[48–50]

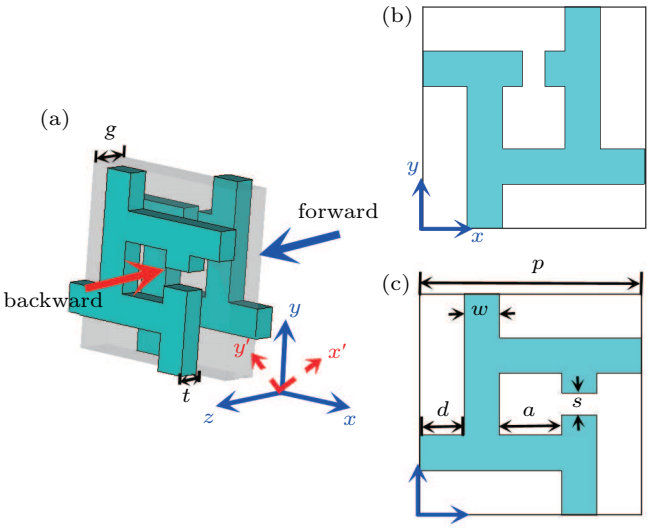


Fig. 1. (a) A unit cell of bi-layer windmill-shaped resonators with blue and red arrows indicating the forward and backward incidences, respectively. (b) and (c) The first and second layers of the unit cell.

Based on the design principles the bi-layer windmill-shaped resonator is proposed and shown in Fig. 1. Figure 1(a) presents the perspective view of a unit cell of this resonator, where the two windmill-shaped metallic layers are separated ($g = 70$ nm) by a silicon oxide dielectric spacer layer with a permittivity of $\varepsilon_{\text{sio2}} = 2.1$. The windmill-shaped metallic layers are made of silver with a Drude-type dispersion, for which the plasma and collision frequencies are $\omega_{\text{p}} = 1.367 \times 10^7$ rad/s and $\gamma = 7.73 \times 10^{13}$ rad/s, respectively, and the high-frequency bulk permittivity $\varepsilon_{\infty} = 6.0$. The blue and red arrows indicate that the x- and y-polarized plane waves propagate along the forward ($+z$) and backward ($-z$) directions, respectively. Figures 1(b) and 1(c) respectively show the first and second layers of the windmill-shaped resonators with the period $p = 500$ nm. The other geometric parameters of the windmill-shaped resonator are set as $t = 40$ nm, $w = 80$ nm, $d = 100$ nm, and $s = 50$ nm.

3. Results and discussion

The simulated forward and backward transmission coefficients are shown in Figs. 2(a) and 2(b) with three resonant peaks labeled I, II, and III at 195, 260, and 309 THz, respectively. In Fig. 2(a), the x-polarized incident plane wave is mostly transformed into a y-polarized output plane wave when it propagates along the forward ($+z$) direction. Consequently, the cross-polarization T_{yx}^{f} reaches 0.75, 0.85, and 0.80 in resonant modes I, II, and III, respectively, and the co-polarization T_{xx}^{f} remains less than 0.1 at all operating frequencies from 195 THz to 309 THz. In addition, a y-polarized incident plane wave is mostly forbidden to pass through the bi-layer windmill-shaped metamaterial when it propagates along the forward ($+z$) direction. Consequently, both the cross-polarization T_{xy}^{f} and co-polarization T_{yy}^{f} maintain low transmission coefficients of less than approximately 0.1, from 195 THz to 309 THz. By contrast, Fig. 2(b) shows that the incident plane wave propagates along the backward ($-z$) direction, and the y-polarized incident plane wave is transformed into an x-polarized output plane wave with high-efficiency transmission coefficients, which satisfy $T_{xy}^{\text{b}} = T_{yx}^{\text{f}}$. However, an x-polarized incident plane wave is forbidden from passing through the windmill-shaped metamaterial. Thus, the cross and co-polarization satisfy $T_{yx}^{\text{b}} = T_{xy}^{\text{f}}$ and $T_{xx}^{\text{b}} = T_{yy}^{\text{f}}$. According to the above discussion, we can calculate the polarization conversion rate (PCR) using $\text{PCR} = T_{xy}^2/(T_{xy}^2 + T_{yy}^2)$.[51] Figure 2(c) clearly shows that broadband polarization conversion has been realized with a bandwidth of about 156 THz, i.e., the PCR is greater than 0.9 in the range 192 THz–348 THz. Over this whole resonant frequency band, the y-polarized incident plane wave is transformed into the x-polarized transmitted plane wave, where the co-polarization transmitted electric field T_{yy}^{b} is nearly zero [Fig. 2(b)] when the y-polarized plane wave propagates along the backward direction. Similarly, the x-polarized incident plane wave can be transformed into the y-polarized transmitted plane wave, when the plane wave propagates along the $+z$ direction.

To study the tunable multi-band AT, we calculated the total transmittance and AT parameters using equations $T_x = T_{yx}^2 + T_{xx}^2/T_y = T_{xy}^2 + T_{yy}^2$ and $\Delta T_x = T_x^{\text{f}} - T_x^{\text{b}}/\Delta T_y = T_y^{\text{f}} - T_y^{\text{b}}$, and the results are presented in Figs. 3(a)–3(c). Figure 3(a) shows that the transmittance of the x-polarized incident plane wave reaches 0.58, 0.74, and 0.62, at 195, 260, and 309 THz, respectively, when it propagates in the forward direction. However, the transmittance remains less than 0.1 when the x-polarized incident plane wave propagates in the backward direction. The differences between the forward and backward directions result in high AT parameters of approximately 0.52,

0.73, and 0.62 at 195, 260, and 309 THz, i.e., the x polarized incident plane wave can pass through the bi-layer windmill-shaped metamaterial in the forward direction at these resonant frequencies. From Figs. 3(b) and 3(c), we find that the y-polarized incident plane wave can pass through the bi-layer windmill-shaped metamaterial in the backward direction.

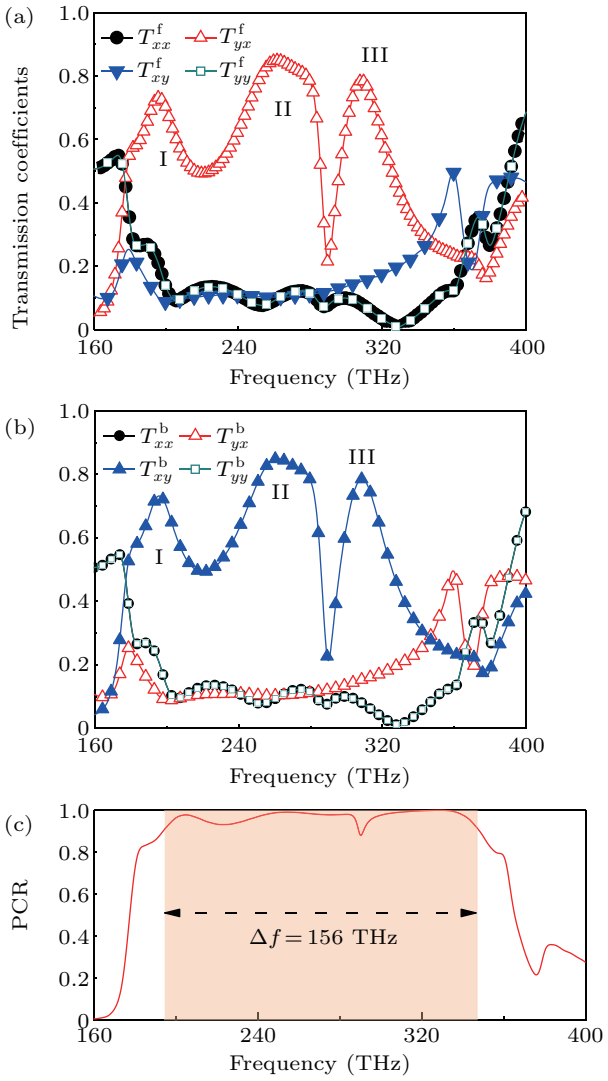


Fig. 2. Simulated transmission coefficients of windmill-shaped resonators, when x- and y-polarized plane waves incident along the (a) forward and (b) backward directions, respectively. I, II, and III show three resonances at 195 THz, 260 THz, and 309 THz, respectively.

By studying the geometric parameters of the windmill-shaped metamaterial, we found that the multi-band AT can be flexibly tuned. First, Fig. 4(a) shows that the size s can easily tune resonant modes II and III, i.e., when s increases from 0 nm to 140 nm, the AT parameters decrease from 0.72 to 0. Meanwhile, the AT parameters increase from 0 to 0.72, and the operation bands of the AT are also broadened in resonant mode III. In addition, Fig. 4(b) shows that the gap g between the first and second layers can tune resonant modes I and III, i.e., when g increases from 40 nm to 250 nm, the AT parameters decrease. A new resonant mode IV is induced when g is increased. Resonant mode IV results in opposite polarization conversions and the AT phenomenon at 343 THz, where the x-polarized incident plane wave can be transformed into a y-polarized output plane wave when it propagates in the backward direction and the maximum AT parameter is -0.6 when $g = 190$ nm. In other words, when $g = 190$ nm, the x-polarized incident plane wave can pass through this bi-layer windmill-shaped metamaterial along the backward ($-z$) direction, which is opposite to resonant modes I, II, and III.

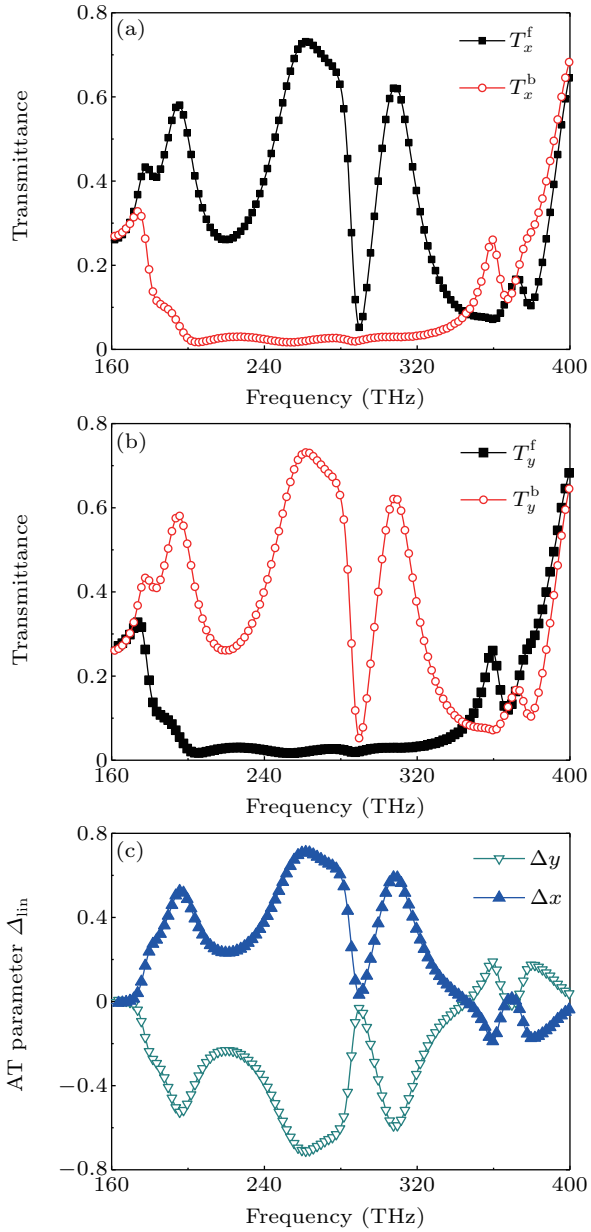


Fig. 3. (a) and (b) The calculated total transmittances for x- and y-polarized excitations propagating along the forward and backward directions. (c) The AT parameters for the designed windmill-shaped resonators. Solid and hollow triangular lines correspond to the AT of the x- and y-polarized plane waves, respectively.

To understand the physical mechanism of the multi-band AT phenomenon, we studied the surface current distributions of this bi-layer windmill-shaped metamaterial in resonant modes I, II, III, and IV. The horizontal red arrows in Figs. 5(a)–5(c) represent the x-polarized incident plane wave.

Figure 5(a) shows that resonant mode I at 195 THz is induced by a design that is parallel to the split arms. Figure 5(b) shows that resonant mode II at 260 THz is induced by the center split rings, identical to the traditional split-ring resonators (SRRs) without windmill-shaped arms.[21,43,49,52] The surface current passes through the spilled s and results in a magnetic dipole resonance; thus, resonant mode II can be easily tuned by changing the size of s. Figure 5(c) shows that resonant mode III at 309 THz is also induced by the design of the windmill-shaped arms, in contrast to resonant mode I, where the surface focuses on the two corners of the L-shaped arms, which are included and parallel to the split arms; therefore, the parameter s can tune resonant mode III. In other words, resonant modes I, II, and III are induced by an x-polarized incident plane wave propagating in the forward direction, resulting in the x-polarized plane wave passing through the bi-layer windmill-shaped metamaterial along the forward ($+z$) direction and transformation to the y-polarized output plane wave. Figure 5(d) shows that resonant mode IV at approximately 343 THz is induced when the y-polarized incident plane wave propagates in the forward direction, and the surface current distributions are localized on the L-shaped arms, which are perpendicular to the spilled arms. In addition, resonant mode IV can only be activated when the gap g increases and the x polarized incident plane wave can only pass through the metamaterial along the backward ($-z$) direction, which results in a negative AT parameter in resonant mode IV in Fig. 4(b).

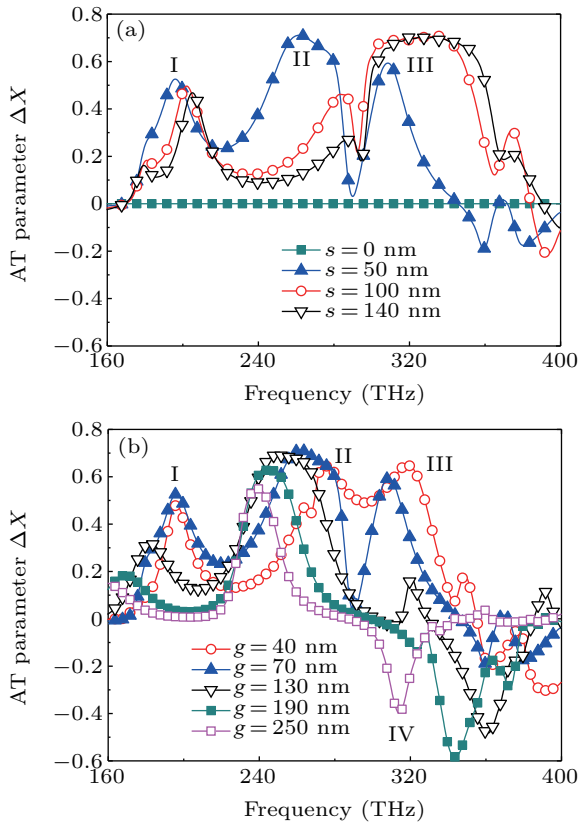


Fig. 4. The tunable AT effect by changing the (a) spilled width s and (b) gap g between the first and second layers.

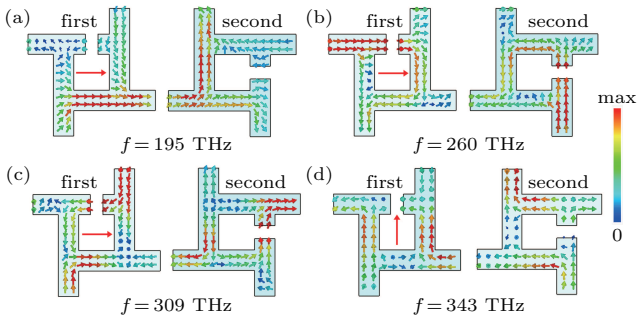


Fig. 5. Current distributions of the multi-band resonant modes at polarization conversion peaks for forwarding propagation. (a)–(c) Simulated current distributions at 195, 260, and 309 THz for x-polarized incidence. (d) Simulated current distributions at 343 THz for y-polarized incidence.

Finally, we also consider the effect of the geometric parameters p and d on the AT parameter. In Fig. 6(a), when the period p increases from 500 nm to 800 nm, the couplings among neighboring periods decrease, and thus the resonances in modes I, II, and III are weakened, which results in a decrease in the AT parameters. In Fig. 6(b), we first set $p = 500$ nm, but set $d = 0$ nm and 100 nm. When $d = 0$ nm, the traditional SRRs without windmill-shaped arms are substituted for our bi-layer windmill-shaped metamaterial, and consequently, the AT parameter only appears at 260 THz (resonant mode II). Further, when d is increased to 200 nm, the period also increases and, consequently, the AT parameter decreases.

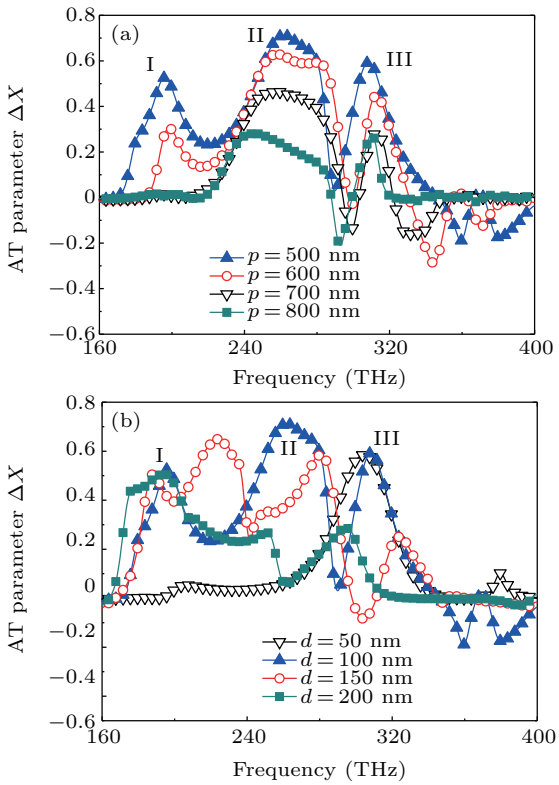


Fig. 6. Calculated AT parameters of the bi-layered windmill-shaped split-ring resonators for different (a) periods p and (b) windmill arm distances d.

4. Conclusion

In this study, we proposed a bi-layer windmill-shaped metamaterial that is different from traditional SRRs, as it can

induce more resonant modes and result in multi-band AT in linearly polarized plane waves. The AT parameters reach 0.58, 0.74, and 0.62 at 195, 260, and 309 THz, respectively. Furthermore, the multi-band AT can be tuned freely by changing the geometric parameters s and g. When $g = 190$ nm, a reversed AT was realized at 343 THz with the AT parameter reaching -0.6. To further understand the physical mechanism, the surface current distributions of this bi-layer windmill-shaped metamaterial are presented for the underlying resonant modes I, II, III, and IV, respectively. It is believed that the multi-band AT effects will be applied as polarization rotators and switches in the field of optical nano-devices.

References

[1] Wu J Y, Xu X F and Wei L F 2020 *Chin. Phys. B* **29** 94202
[2] Chen L, Li H, Hao W, Yin X and Wang J 2020 *Chin. Phys. B* **29** 84210
[3] He Z H, Zhao J B, Yao H and Chen X 2019 *Acta Phys. Sin.* **68** 214302 (in Chinese)
[4] Liu S G, Zhao Y C and Zhao D 2019 *Acta Phys. Sin.* **68** 234301 (in Chinese)
[5] Wu Q N, Lan F, Tang X P and Yang Z Q 2015 *Chin. Phys. Lett.* **32** 107801
[6] Wei Z, Cao Y, Fan Y, Yu X and Li H 2011 *Appl. Phys. Lett.* **99** 221907
[7] Lévesque Q, Makhsiyan M, Bouchon P, Pardo F, Jaeck J, Bardou N, Dupuis C, Haïdar R and Pelouard J L 2014 *Appl. Phys. Lett.* **104** 111105
[8] Wu S, Zhang Z, Zhang Y, Zhang K, Zhou L, Zhang X and Zhu Y 2013 *Phys. Rev. Lett.* **110** 207401
[9] Hao J, Yuan Y, Ran L, Jiang T, Kong J A, Chan C T and Zhou L 2007 *Phys. Rev. Lett.* **99** 063908
[10] Sun Z C, Yan M Y and Xu B J 2020 *Chin. Phys. B* **29** 104101
[11] Wu L X, Li X, and Yang Y J 2019 *Acta Phys. Sin.* **68** 234201 (in Chinese)
[12] Yang X, Wei Ti, Chen F, Gao F, Du J and Hou Y 2020 *Chin. Phys. B* **29** 107303
[13] Gao F, Lu D, Zhang R K, Wang H T, Wang W and Ji C 2016 *Chin. Phys. Lett.* **33** 24203
[14] Lin B Q, Lv L T, Gao J X, Wang Z L, Huang S Q and Wang Y W 2020 *Chin. Phys. B* **29** 104205
[15] Shi J X, Zhang W C, Xu W, Zhu Q, Jiang X, Li D D, Yan C C and Zhang D H 2015 *Chin. Phys. Lett.* **32** 94204
[16] Chen J, Yang M S, Li Y D, Cheng D K, Guo G L, Jiang L, Zhang H T, Song X X, Ye Y X, Ren Y P, Ren X D, Zhang Y T and Yao J Q 2019 *Acta Phys. Sin.* **68** 247802 (in Chinese)
[17] Zhu Y, Tang B and Jiang C 2019 *Appl. Phys. Express* **12** 032009
[18] Wang R, Li L, Tian H, Liu J, Liu J, Tian F, Zhang J and Sun W 2018 *Opt. Commun.* **427** 469
[19] Li Y, Dong G, Zhao R, Wang K, Zhou S, Sun L, Li P, Zhu Z, Guan C and Shi J 2018 *J. Phys. D Appl. Phys.* **51** 285105
[20] Li T, Hu F R, Qian Y X, Xiao J, Zhang L H, Zhang W T and Han J G 2020 *Chin. Phys. B* **29** 024203
[21] Zhang L, Zhou P, Chen H, Lu H, Xie H, Zhang L, Li E, Xie J and Deng L 2016 *Sci. Rep.* **6** 33826
[22] Kenanakis G, Xomalis A, Selimis A, Vamvakaki M, Farsari M, Kafesaki M, Soukoulis C M and Economou E N 2015 *ACS Photon.* **2** 287
[23] Zhao Y, Belkin M A and Alu A 2012 *Nat. Commun.* **3** 870
[24] Wang Y H, Shao J, Li J, Zhu M J, Li J and Dong Z G 2016 *J. Opt.* **18** 055004
[25] Aba T, Qu Y, Wang T, Chen Y, Li H, Wang Y, Bai Y and Zhang Z 2018 *Opt. Express* **26** 1199
[26] Xu H X, Wang G M, Qi M Q, Cai T and Cui T J 2013 *Opt. Express* **21** 24912
[27] Tang D F, Wang C, Pan W K, Li M H and Dong J F 2017 *Opt. Express* **25** 11329
[28] Wang S, Wei G, Wang X, Qin Z, Li Y, Lei W, Jiang Z H, Kang L and Werner D H 2018 *Appl. Phys. Lett.* **113** 081904
[29] Bai Y, Wang T, Ullah H, Qu Y, Abudukelimu A and Zhang Z 2019 *Annalen der Physik* **531** 1800469
[30] Jiang H, Zhao W and Jiang Y 2017 *Opt. Express* **25** 19732
[31] Zhao J, Song J, Xu T, Yang T and Zhou J 2019 *Opt. Express* **27** 9773
[32] Shi J, Liu X, Yu S, Lv T, Zhu Z, Ma F H and Cui T J 2013 *Appl. Phys. Lett.* **102** 191905
[33] Xiao Z Y, Liu D J, Ma X L and Wang Z H 2015 *Opt. Express* **23** 7053
[34] Fu T, Liu X X, Wen G H, Sun T Y, Xiao G L and Li H O 2021 *Chin. Phys. B* **30** 014201
[35] Kim M, Yao K, Yoon G, Kim I, Liu Y and Rho J 2017 *Adv. Opt. Mater.* **5** 1700600
[36] Menzel C, Helgert C, Rockstuhl C, Kley E B, Tunnermann A, Pertsch T and Lederer F 2010 *Phys. Rev. Lett.* **104** 253902
[37] Li Z, Chen S, Tang C, Liu W, Cheng H, Liu Z, Li J, Yu P, Xie B, Liu Z and Li J and Tian J 2014 *Appl. Phys. Lett.* **105** 201103
[38] Wang Y H, Shao J, Li J, Liu Z, Li J Q, Dong Z G and Zhai Y 2015 *J. Appl. Phys.* **117** 173102
[39] Li, Z, Chen S, Liu W, *et al*. 2015 *Plasmonics* **10** 1703
[40] Wang Y H, Jin R C, Li J, Li J Q and Dong Z G 2018 *Opt. Express* **26** 3508
[41] Tang D F, Wang C Pan W K Li M H and Dong J F 2017 *Opt. Express* **25** 11329
[42] Li X, Feng R and Ding W 2018 *J. Phys. D Appl. Phys.* **51** 145304
[43] Kang M, Wang H T and Zhu W 2014 *Opt. Express* **22** 25679
[44] Zhao J, Fu Y, Liu Z and Zhou J 2017 *Opt. Express* **25** 23051
[45] Huang X, Yang D and Yang H 2014 *J. Appl. Phys.* **115** 103505
[46] Huang S, Xie Z, Chen W, Lei J, Wang F, Liu K and Li L 2018 *Opt. Express* **26** 7066
[47] Cao T, Wei C and Zhang L 2014 *Opt. Mater. Express* **4** 1526
[48] Menzel C, Rockstuhl C and Lederer F 2010 *Phys. Rev. A* **82** 053811
[49] Huang C, Feng Y, Zhao J, Wang Z and Jiang T 2012 *Phys. Rev. B* **85** 195131
[50] Zhang C, Cheng Q, Yang J, Zhao J and Cui T J 2017 *Appl. Phys. Lett.* **110** 143511
[51] Zhao J X, Song J L, Zhou Y, Zhao R L, Liu Y C and Zhou J H 2020 *Chin. Phys. B* **29** 94205
[52] Chen K, Feng Y, Cui L, Zhao J, Jiang T and Zhu B 2017 *Sci. Rep.* **7** 42802